A personalized mathematical tool for neuro-oncology: a clinical case study

Agosti, A.; Giverso, C.; Faggiano, E.;Stamm,A.; Ciarletta, P.

MOX, Dipartimento di Matematica
Politecnico di Milano, Via Bonardi 9 - 20133 Milano (Italy)

mox-dmat@polimi.it   http://mox.polimi.it

A personalized mathematical tool for neuro-oncology: a clinical case study

A. Agosti[♯], C. Giverso[‡], E. Faggiano[♭], A. Stamm[♯, ♮, ⋄] and P. Ciarletta[♯]

February 21, 2018

[♯] MOX– Modellistica e Calcolo Scientifico, Dipartimento di Matematica "F. Brioschi"
Politecnico di Milano, via Bonardi 9, 20133 Milano, Italy

[‡] Dept. of Mathematical Sciences, Politecnico di Torino,
Corso Duca degli Abruzzi 24, 10129 Torino, Italy

[♭] Dept. of Civil Engineering and Architecture, University of Pavia,
Via Adolfo Ferrata, 3, 27100 Pavia, Italy

[♮] Computational Radiology Lab, Boston Children's Hospital
Harvard Medical School, 300 Longwood Ave, 02115 Boston, MA, USA

[⋄] Center for Analysis, Decisions, and Society, Human Technopole, Palazzo Italia
Via Cristina Belgioioso, 20157 Milano, Italy

Abstract

This work evaluates the predictive ability of a novel personalised computational tool for simulating the growth of brain tumours using the neuroimaging data collected during one clinical case study. The mathematical model consists in an evolutionary fourth-order partial differential equation with degenerate motility, in which the spreading dynamics of the multiphase tumour is coupled through a growth term with a parabolic equation determining the diffusing oxygen within the brain. The model also includes a reaction term describing the effects of radiotherapy, that is simulated in accordance to the clinical schedule. We collect Magnetic Resonance (MRI) and Diffusion Tensor (DTI) imaging data for one patient at given times of key clinical interest, from the first diagnosis of a giant glioblastoma to its surgical removal and the subsequent radiation therapies. These neuroimaging data allow reconstructing the patient-specific brain geometry in a finite element virtual environment, that is used for simulating the tumour recurrence pattern after the surgical resection. In particular, we characterize the different brain tissues and the tumour location from MRI data, whilst we extrapolate the heterogeneous nutrient diffusion parameters and cellular mobility from DTI data.
The numerical results of the simulated tumour are found in good qualitative and quantitative agreement with the volume and the boundaries observed in MRI data. Moreover, the simulations point out a consistent regression of the tumour mass in correspondence to the application of radiotherapy, with an average growth rate which is of the same order as the

one calculated from the neuroimaging data. Remarkably, our results display the highest Jaccard index of the tumour region reported in the biomathematical literature.

In conclusion, this work represents an important proof-of-concept of the ability of this mathematical framework to predict the tumour recurrence and its response to therapies in a patient-specific manner.

1 Introduction

Glioblastoma multiforme (GBM) is the most aggressive subtype of glioma, a type of primary brain tumour arising from the glial cells of the nervous system. The median survival of patients with GBM is less than one year, rising up to 15-16 months for those treated with the standard protocol of surgery followed by adjuvant chemotherapy and radiation treatment [26, 25, 8]. Its poor prognosis is related to the surgical limitations in performing a complete resection, that is feasible only in a low percentage of cases, and to the infiltrative nature of the tumour cells, hindering the precise detection of GBM boundaries, both with by neuroimaging and by intra-operative techniques [35, 37]. Consequently, the surgical resection is often ineffective, and GBM almost invariably recurs independently from the post-operative treatments. Waiting for novel therapeutic approaches, improving the patient survival rate and the quality of life requires screening methods for the earlier detection of GBM, as well as a deeper understanding of its evolution dynamics prediction, in order to target surgical procedures and treatments.

The *magnetic resonance imaging* (MRI) is the technique of election in detecting brain tumours, providing a detailed microscopic reconstruction of the brain. Nonetheless, it fails in giving insights on its realistic infiltration, that is very often well beyond the detected boundary. The GBM spreading is highly influenced by the local heterogeneity and anisotropy of the brain tissue. In particular, whilst the motion of cells inside the cerebrospinal fluid is driven by isotropic unconfined diffusion, the tumour cells migrate rapidly inside the constrained domain of the white matter (made by bundles of myelinated nerve fibres) preferably along the direction of the nerve tracts [24, 23, 46, 20, 64], whereas they move slowly in the grey matter (consisting, primarily, of neuronal cell bodies, glial cells, synapses and capillaries), due to the lack of a preferential expansion direction in the microstructure.

The advent of Diffusion Tensor Imaging (DTI) has allowed clinicians to infer new insights on the local alignment of the brain fibers within each voxel (i.e. a volumetric image element), by deriving the principal direction of water diffusion, that are also relevant for cell migration [46, 20, 64]. Despite providing a useful indication on the brain microstructure, the DTI does not give a direct measurement of the extent of cell migration, which is regulated by complex chemical and mechanical cues [32, 50]. Nonetheless the DTI technology paves the way to improve patient-specific strategies of GBM treatment, giving additional information about the brain micro–structure of each patient.

In combination with the biomathematical modeling of GBM evolution, such neuroimaging techniques open the possibility to build predictive and quantitative tools for the personalised investigation of the spatio-temporal evolution and infiltration of GBM. The resulting insights allow testing different therapeutic strategies in order to improve the treatment outcomes. This works goes beyond the mathematical state-of-the-art for modeling GBM growth, that is collected in the exhaustive reviews [26, 3]. Swanson et al. [54] first described the GBM cells growth through a simple reaction-diffusion equation, with either a heterogeneous diffusion coefficient (i.e. a piecewise-function with two different constant values in each region) [54, 56] or an anisotropic and heterogeneous diffusion tensor [30] derived from DTI. Later improvements included the effect of therapies, defining the so-called Proliferation-Invasion-Radiation-Therapy model [47, 17], in which a loss term representing cell-killing by radiation was used to predict re-

2

sponse to external beam radiotherapy on a patient-specific basis. These approaches have been tested by comparing the predictions of the mathematical model with the measured tumour growth [52, 48, 6, 33, 38, 39] and its recurrence after resection [55, 57].

Other modelling approaches used a diffusion tensors of the *Fokker-Planck* form (instead of the standard *Fickian* form used in Swanson's models), derived through the parabolic scaling limit of the mesoscopic transport equations [41, 29, 21, 22]. These models have introduced a systematic procedure for connecting the DTI data to parameters in the macroscopic model, showing a good ability to reproduce the tumour evolution, at least in those situations in which the tumour is somewhat regular [53]. However, both classes of diffusive models neglect the generation and accumulation of forces inside the tumour, at the interface between the host and the malignant tissue and inside the healthy tissue.

The first attempt to include such mechanical cues inside a mathematical GBM model was done in [13] defining a mass effect, that results from the physical pressure and includes the effects of the deforming tissue. Mechanical models have been further refined in [9, 28], performing numerical simulations using atlas data (which provides a general map of a human brain that is not specific to a particular patient), to be compared to the clinically observed growth. Notwithstanding, these mechanical models considered neither the effect of therapies on tumour growth nor its recurrence after incomplete resection, and describe the tumour mass made by a single constituent.

Multiphase mixture models represents a more realistic descriptions of GBM evolution at a macroscopic scale [4, 11]. They consider the tumour as a saturated medium [10], comprising at least one solid phase (e.g. cells, extracellular matrix, etc) and one liquid phase (e.g. water) [11, 61, 19, 4]. We recently proposed a novel multiphase GBM model based on a phase-field approach [14]. Later improvements [2] allowed us accounting for the cell motion along the white matter fibers and for the response of tumour mass to chemotherapy and radiotherapy. In this work, we make a step forward towards the integration of clinical neuroimaging data within this personalised mathematical framework. In particular, we introduce a numerical approach in order to assess the predictive ability of the model to reproduce the tumour growth dynamics observed in a clinical case study. This work is organized as follows. In section 2 we summarize the main aspects of the multiphase continuous mathematical model of GBM growth [2], used to simulate the specific clinical case of a patient diagnosed with a *giant cell glioblastoma* (i.e., a subtype of glioblastoma multiforme characterized by a predominance of multinucleated giant cells [34]). We follow its evolution from the surgical removal to the end of the adjuvant radiotherapy, consisting of 5 weeks of daily sessions during five days per week, and starting 40 days after surgery). In section 3 we describe the new numerical strategy to elaborate the neuroimaging data, collected at given times of key clinical interest by the *Istituto Neurologico Carlo Besta* (Milan, Italy). In section 4 we define an original procedure to include such patient-specific data in the model, by defining and tuning adaptively its relevant parameters. We later perform numerical simulations of the tumour re-growth after surgery and radiotherapy, evaluating in section 5 the predictive ability of the model against the clinical data. The main results are discussed in the last section, together with few concluding remarks.

2   Mathematical model

The GBM evolution is described by the continuum diffuse-interface multiphase model proposed in [2]. Specifically, the tumour mass is represented as a binary, saturated, closed mixture of two incompressible constituents [11, 12, 14]: the *cellular phase* accounting for tumour cells and the *liquid phase* representing host healthy cells, dead tumour cells and the interstitial fluid with possibly nutrients or other chemicals dispersed inside it. Since the cells are mostly composed

3

by water, it is possible to assume that the true mass densities [10] are constant and equal to the water density, so that the evolution can be represented in terms of their volume fractions: the tumour volume fraction ϕ and the liquid/host volume fraction $\phi_\ell = (1 - \phi)$.

The tumour expands either by cell motion inside the host tissue, guided by both mechanical and chemical cues, or by cell proliferation and death, that are related to nutrients availability and of GBM response to therapies. In particular, we consider here oxygen as the only chemical species coupled in cell production/loss and we restrict our analysis to the response only to radiotherapy. The evolution of the oxygen concentration inside the brain is described by a parabolic equation, accounting both for its diffusion inside the heterogeneous and anisotropic brain tissue, and for its uptake, at a constant rate δ_n, by the neoplastic cells and for the release, at a rate S_n, from an homogeneously distributed vasculature filling the available healthy/liquid space. Without loss of generality, we consider the dimensionless concentration of the diffusing nutrient, $n(\mathbf{x}, t)$, normalized with respect to the typical physiological concentration n_s in the capillaries.

After enforcing the mechanical balance laws, the model reduces to the following system of coupled partial differential equations, representing the spatio-temporal evolution of the GBM and nutrients [2]:

$$\frac{\partial \phi}{\partial t} = \nabla \cdot \left(\frac{\phi(1 - \phi)^2}{M_0} \boldsymbol{T} \nabla(f(\phi) - \epsilon^2 \Delta \phi) \right) - \nabla \cdot (k_n \phi n_s \boldsymbol{T} \nabla n)$$
$$+ \nu \phi [n - \delta]_+ (1 - \phi) - \nu_d \phi [\delta - n]_+ - k_R(t) \phi \,, \tag{1a}$$

$$\frac{\partial n}{\partial t} = \nabla \cdot (\boldsymbol{D} \nabla n) - \delta_n \phi n + S_n (1 - n)(1 - \phi) \,. \tag{1b}$$

The first term on the r.h.s. of eq. (1a) reproduces the motion of cells in response to the mechanical stress inside the tumour mass. Specifically M_0 is a friction parameter, $\boldsymbol{T}$ is a positive definite symmetric tensor representing the preferential directions of white matter fiber tracts, $f(\phi)$ is a phenomenological function describing the excess of stress in the tissue due to cell-cell mechanical interactions[12, 11, 4] whereas the term $\epsilon^2 \Delta \phi$ takes into account the non-local intermixing and adhesion forces that generate a sort of surface tension between the tumour and the host tissue, controlling the thickness of the moving diffuse interface that represents the expanding GBM. In the present work, we assume that $f(\phi)$ takes the form of a single-well Lennard-Jones type potential

$$f(\phi) = E \frac{\phi^2(\phi - \phi_e)}{1 - \phi}, \tag{2}$$

where E is the Young modulus of the cancerous phase [11] and ϕ_e is the volume fraction corresponding to the state of equilibrium or undeformed state (i.e., the threshold value for which no action is exerted on the neighbours cells). Along with mechanical cues, tumour cells also move in response to chemical factors, such as nutrients, in a process called chemotaxis. The second term on the r.h.s of eq. (1a), precisely, takes into account the chemotactic motion of GBM cells towards higher concentration of oxygen, following the preferential directions of white matter fibers, according to the specific chemotactic parameter k_n and the maximum amount of oxygen released by the vasculature n_s. The nutrient availability not only influences the motion of tumour cells but also guides their proliferation and death, accordingly to the third and fourth terms on the r.h.s. of eq. (1a), where $[\cdot]_+$ stands for the positive part of its argument, ν and ν_d are the neoplastic cells proliferation and death rates respectively and δ is a threshold value for hypoxia. The proliferation term also encapsulates contact inhibition mechanisms by enforcing the saturation constraint. Finally, the last term on the r.h.s of eq. (1a) represents cell death in response to the application of the external beam radiation therapy. The mass sink term is taken proportional to the GBM volume fraction with a death rate $k_R(t)$, which follows the

4

temporal profile of the therapy schedule [43]. The specific radiotherapy protocol considered in this work consists of fractionated focal irradiation at a total daily dose d of 2 Gy, five consecutive days per week. The patient undertook 25 sessions before interrupting the treatment for severe clinical complications. Therefore, referring to the linear-quadratic (LQ) model [58], $k_R(t)$ can be modelled by the following piecewise constant function:

$$k_R(t) = \begin{cases} \alpha d + \beta d^2 & t_{2i} \leq t \leq t_{2i+1} \\ 0 & \text{otherwise} \end{cases} \tag{3}$$

where α [Gy^{-1}] and β [Gy^{-2}] are two tissue-dependent parameters, called respectively the *linear* and *quadratic* coefficients for cell kill [47, 49], and t_{2i} and t_{2i+1}, with $i = 0, ..., 4$, are respectively the days at the beginning and at the end of each weakly radiotherapy periods.

We remark that both the diffusion of oxygen and the motion of cells are represented by heterogeneous and anisotropic tensors, $\boldsymbol{D}$ and $\boldsymbol{T}$ respectively, that can be inferred by the patient specific DTI data. The oxygen released by the vasculature is carried by the interstitial fluid diffusing inside the extracellular space, so that the local values of tensor $\boldsymbol{D}$ can be directly obtained by the diffusion tensor of water from the DT images. We also assume that also tumour cells travel in the extracellular space either in an isotropic manner if they are in a liquid region or following the preferential directions of white matter fibers. However, the ability of cells to directly move along the fiber tracks is enhanced with respect to random water motion along the same path. Therefore we choose the tensor $\boldsymbol{T}$ in order to keep the same eigenvectors of the tensor $\boldsymbol{D}$ with an enhanced cell motion along preferential directions characterized by a tuning parameter $r > 1$, as done in [30, 2]. Specifically, denoting by λ_i and $\boldsymbol{e}_i$ (with $i = 1, 2, 3$) the descending ordered eigenvalues and the corresponding eigenvectors of $\boldsymbol{D}$, we define

$$\boldsymbol{T} = \frac{1}{\hat{T}_{av}}\hat{\boldsymbol{T}}, \quad \text{with} \quad \hat{T}_{av} = \frac{1}{3}tr(\hat{\boldsymbol{T}}) \quad \text{and} \quad \hat{\boldsymbol{T}} = a_1(r)\lambda_1\boldsymbol{e}_1 \otimes \boldsymbol{e}_1 + a_2(r)\lambda_2\boldsymbol{e}_2 \otimes \boldsymbol{e}_2 + a_3(r)\lambda_3\boldsymbol{e}_3 \otimes \boldsymbol{e}_3,$$

where $a_i(r)$ are functions of the anisotropy controlling factor r and depend on the linear (c_ℓ), planar (c_p) and spherical anisotropy coefficients (c_s), defined as follows

$$\begin{pmatrix} a_1(r) \\ a_2(r) \\ a_3(r) \end{pmatrix} = \begin{pmatrix} r & r & 1 \\ 1 & r & 1 \\ 1 & 1 & 1 \end{pmatrix} \begin{pmatrix} c_\ell \\ c_p \\ c_s \end{pmatrix}, \qquad c_\ell = \frac{\lambda_1 - \lambda_2}{\lambda_1 + \lambda_2 + \lambda_3}, \qquad c_p = \frac{2(\lambda_2 - \lambda_3)}{\lambda_1 + \lambda_2 + \lambda_3}, \qquad c_s = \frac{3\lambda_3}{\lambda_1 + \lambda_2 + \lambda_3}.$$

Finally the system (1) is integrated with proper initial and boundary conditions, that will be discussed in the Section 4.

3 Integration of the imaging data into a virtual computational environment

MR images were acquired at four events: pre-surgery (*PreSurg*), i.e. one day before the surgery; post-surgery (*PostSurg*), i.e. 2 days after the surgery; pre-radiotherapy (*PreRad*), i.e. 34 days after the surgery; post-radiotherapy (*PostRad*), i.e. 79 days after the surgery.

Three types of MR images were acquired at the PreSurg event: (i) a T_1-weighted MR image at 1mm × 1mm × 1mm spatial resolution, useful to depict the structural anatomy of the patients brain; (ii) a FLAIR (FLuid-Attenuated Inversion Recovery) image at 1mm × 1mm × 0.5mm spatial resolution, useful to delineate the outline of the tumour and peri-tumoural rim by suppressing signal from cerebrospinal fluid (CSF); (iii) a set of 140 diffusion-weighted images at 2mm×2mm×2mm spatial resolution with anterior-posterior phase encoding direction, including

16 images without diffusion weighting (referred to as B_0 images), 20 images with a b-value of $700s/mm^2$ and 20 diffusion-sensitising directions, 40 images with a b-value of $1500s/mm^2$ and 40 diffusion-sensitising directions and 64 images with a b-value of $3000s/mm^2$ and 64 diffusion-sensitising directions. All 124 diffusion-sensitising directions were sampled uniformly on the hemisphere. An additional B_0 image was acquired with reversed phase encoding direction, i.e. posterior-anterior encoding, for helping in geometric distortion correction. At the PostSurg and PreRad events only the T_1-weighted and the FLAIR MR images were collected, whereas only the T_1-weighted MR image was collected at the PostRad image. The fact that no diffusion image has been collected after the operation event forced us to artificially reconstruct the diffusion field after the deformation induced by the removal of the tumour mass on the neighboring tissues after the surgery. All MRI data were processed using the ANIMA toolbox, unless specified otherwise. The raw diffusion data were preprocessed at each event as follows:

- **Eddy current distortion correction.** This is done by non-linear registration of 140 diffusion images onto the first one, in which each non-linear transformation is computed only in the phase encoding direction.

- **Susceptibility distortion correction.** This is done using the method proposed by [27], which uses forward and backward phase encoding images to estimate susceptibility-induced deformations and correct for them by symmetric block-matching non-linear registration.

- **Denoising.** This is done by blockwise non-local means filtering of each diffusion image according to the methods proposed in [18] and [60].

- **Brain masking.** Two steps have been implemented: (i) a segmentation of the brain is obtained from the T1-weighted structural image by atlas-based squared velocity function non-linear registration [15] and (ii) a projection of the resulting segmentation onto the diffusion space is made via block-matching rigid registration [40, 16].

- **Tensor model estimation.** A simple yet popular model for the diffusion estimation is the tensor model [7] which assumes that water diffuses according to a Gaussian process with zero mean and covariance matrix proportional to the so-called diffusion tensor. The diffusion MR signal is related to the diffusion tensor in an exponential analytical way. Tensors are then estimated from the diffusion images by matrix inversion using the log-signals. The estimated tensors that are not definite positive are replaced by a definite positive tensor extrapolated from neighbouring voxels.

For fair image comparison, all images were projected into the space of the T1-weighted image of the first event (PreSurg). This was done by affine block-matching registration. Specifically, five images were deemed relevant for our tumour model: (i) the brain-masked T1-weighted image which provides a structural picture of the brain; (ii) the brain-masked estimated tensor image composed of single diffusion tensors in each voxel which provides valuable information for nutrient displacements; (iii) the brain-masked FLAIR image which helps in delineating the evolution of the tumour for comparison with our model prediction; (iv) a segmentation of CSF, grey matter, white matter and the background that is obtained via the FAST algorithm proposed by [63] which uses a hidden Markov random field to estimate the segmentation through expectation-maximization, comparing the given images with probabilistic *atlases* relative to the specified anatomical structures. These atlases are general reference images obtained by averaging among the brain structures of different patients. The segmentation procedure is elaborated from the T1-weighted MR images and produces colored labeled images superposed

to the corresponding T1-weighted images (Fig. 1a-d); (v) a manual segmentation of the tumour region (Fig. 1-e), obtained using a segmentation module provided by an open source software called *Slicer3D* [42] starting from the T1-weighted and the FLAIR images.

In Figure 1 we report sagittal slices of the T1-weighted MR images at the PreSurg (1-a) and PostSUrg (1-b) event, with the corresponding segmentation maps of the brain tissues (1-c and 1-d respectively). We also show the manually segmented map of the tumour associated to the PreSurg event (1-e), and the manually segmented maps of the ventricle area interested by deformation at the PreSurg and PostSurg events (1-f), highlighting the deformation undergone by the brain tissues after the surgical removal of the tumour mass.

From Figure 1-a it can be observed that the ventricle filled with CSF is being deformed and enlarged by the presence of the growing tumour mass. From Figures 1-a and 1-b it can be observed how the ventricle filled with CSF and containing the tumour mass at the PreSurg contracts after the surgical removal of the tumour mass. We note moreover from Figure 1-b that some tumour particles are present in the PostSurg image inside the deformed area which was previously filled by the tumour mass, which are highlighted as light white spots and are recognized by the segmentation process as belonging to the white matter tissue (colored in brown), eventually containing CSF (see Figure 1-d). This information is used for reconstructing the diffusion tensor field at the PostSurg event starting from its values acquired at the PreSurg event, and for determining the initial tumour concentration at the PostSurg event.

In particular, in order to characterize the deformation undergone by the brain tissues after the surgery of the tumour mass, we manually identified the ventricle area interested by the enlargement due to the presence of the tumour mass at the PreSurg event and the corresponding area at the PostSurg event, as depicted in Figure 1-f.

4   Numerical Discretization of the GBM model

This section concern the numerical procedure for obtaining a patient-specific virtual environment in finite element simulations.

First, we describe in Section 4.1 the mesh generation technique for integrating the data collected by the MRI and the DTI in the patient-specific brain domain Ω to be used in numerical simulations. In Section 4.2 we summarize the numerical procedure for tuning the model parameters and the initial tumour concentration at the PostSurg event in order to fit the available clinical data. Finally, in Section 4.3 we show how to reconstruct the diffusion tensor from the data collected at the PreSurg stage, by considering the deformation of the brain tissues after the tumour mass removal, due to a lack of DTI data at the PostSurg event.

4.1   Finite element discretization and meshes generation

The eqs. (1a),(1b) have been solved using the finite element scheme introduced in [2], that uses a discrete variational inequality for projecting the solution in each mesh element onto the space of first-order polynomials with positive values. This projection aims at recovering the analytical properties of the continuous solution, which can be shown to satisfy a positivity constraint and a separation property from the singular value of the single-well potential. In particular, the scheme is solved by a splitting algorithm on the nodes of the mesh whose associated basis functions span the set on which the degenerate elliptic operator in (1) can be inverted (see also [1] for details).

In order to study the patient-specific tumour evolution we extrapolate from the MR and DT images the brain geometry mesh and additional meshes containing the values of the independent components of the tensors $\mathbf{D}$ and $\mathbf{T}$.
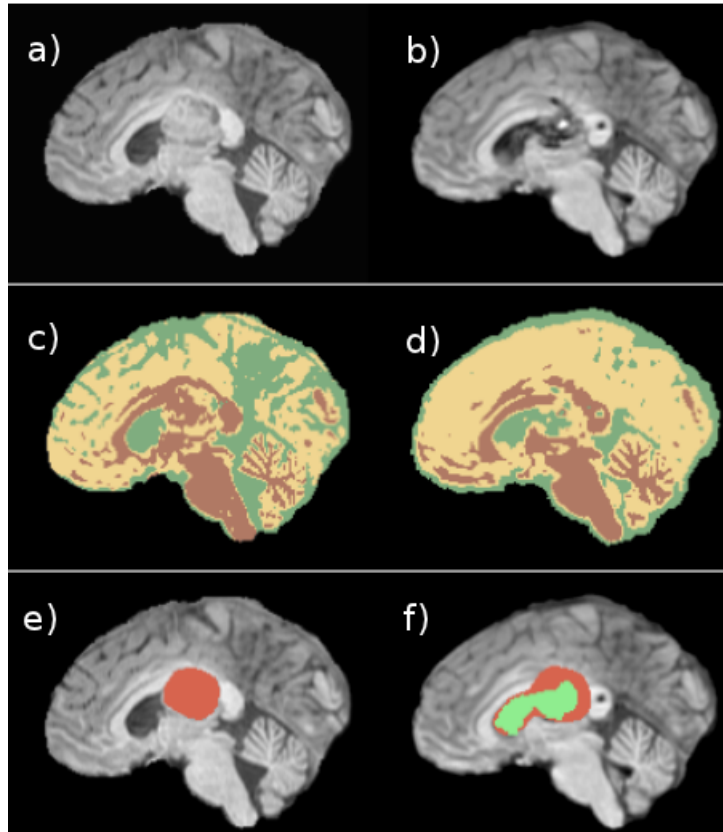
Figure 1: Sagittal slices of T1-weighted MR images with segmentation maps superposed at the PreSurg event (left column) and PostSurg event (right column). a) T1-weighted MR image at the PreSurg event; b) T1-weighted MR image at the PostSurg event; c) Segmented map at the PreSurg event, in which are highlighted white matter (in brown), grey matter (in yellow) and cerebrospinal fluid (in green); d) Segmented map of the brain tissues at the PostSurg event; e) Manually segmented and afterwards smoothed tumour map (in red) at the PreSurg event; f) Manually segmented maps of the ventricle area interested by deformation at the PreSurg (in red) and PostSurg (in green) event.

Table 1: Values of the total volume of the multiphase tumour extensions at the PreSurg, PreRad and PostRad events

	PreSurg	PreRad	PostRad
tumour volume	$17313.6\,mm^3$	$6504.5\,mm^3$	$10973.6\,mm^3$

In particular we extract the external brain and tumour surfaces from the segmentation of the MR images at the PreSurg event, then we generate the surface computational mesh (Fig. 2a-b). After a preliminary smoothing of the segmented maps, we treat the MR images with VMTK [5] (*the Vascular Modeling ToolKit*), a collection of Python libraries and tools, in order to create the computational tetrahedral meshes. First, the external brain and tumour surfaces are extracted from the segmented maps, using the *marching cubes* algorithm. Then, operating multiple surface smoothing and refinement steps, we obtain the surface computational mesh (Fig. 2a-b and 3). Afterwards, the internal tetrahedrons are generated through a constrained Delaunay tetrahedralization of the domain defined by its boundary using the TetGen library [51], and the brain mesh is conveniently refined in the area surrounding the tumour center (Fig. 2c-d). Lastly, the labelled mesh is created exploiting the capabilities of the Visualization Toolkit (VTK) library [65], in order to assign a label to each cell depending on which cerebral tissue the cell barycenter belongs to (Fig. 2e-f).

By analyzing the tumour surface extension reported in Figure 3 we observe that the tumour mass has an ellipsoid-like form, with semiaxes of $23.5, 15.3, 13.6\ mm$ in the x, y, z directions, respectively, and occupies a global volume of about $17313.6\,mm^3$. The volume has been calculated by integrating the characteristic function associated to the tumour segmentation map over the computational mesh. Using the same technique we calculated the volumes of the tumour extension at the PreRad and PostRad events, starting from the manually segmented maps of the tumour. The corresponding values of the tumour volume are reported in Table 1.

We note that the tumour volume at the PostRad event is more than half the volume at the PreSurg event.

We finally generated the additional six meshes, each one representing one independent component of the symmetric water diffusion tensor $\boldsymbol{D}$, starting from the DTI data. These images have been treated in order to give the numerical diffusion value in mm^2/s for each each voxel. The diffusion tensor data are associated to each cell with the same procedure used for the labels, thus creating six different meshes, each one representing one independent component of the symmetric diffusion tensor $\boldsymbol{D}$. At the same time, additional six meshes associated with each independent component of the tensor of preferential directions $\boldsymbol{T}$ are created from the components of $\boldsymbol{D}$, as explained in subsection 2. Figure 4 depicts an axial (z-normal) slice of the DTI data associated to the xx-component of the diffusion tensor (a), with the corresponding meshes associated to the same component of the tensors $\boldsymbol{D}$ (b) and $\boldsymbol{T}$ (c). We note that inside the tumour mass the diagonal values of the tensor $\boldsymbol{D}$ can be an order of magnitude smaller than the diffusion values in the surrounding CSF.

4.2 Tuning of the model parameters and determination of the initial condition

In order to obtain a clinically useful and potentially predictive model, we first have to tune the parameters and the initial tumour concentration at the PostSurg event to fit the available clinical data. We start our analysis considering the set of parameters reported in [2], that fall
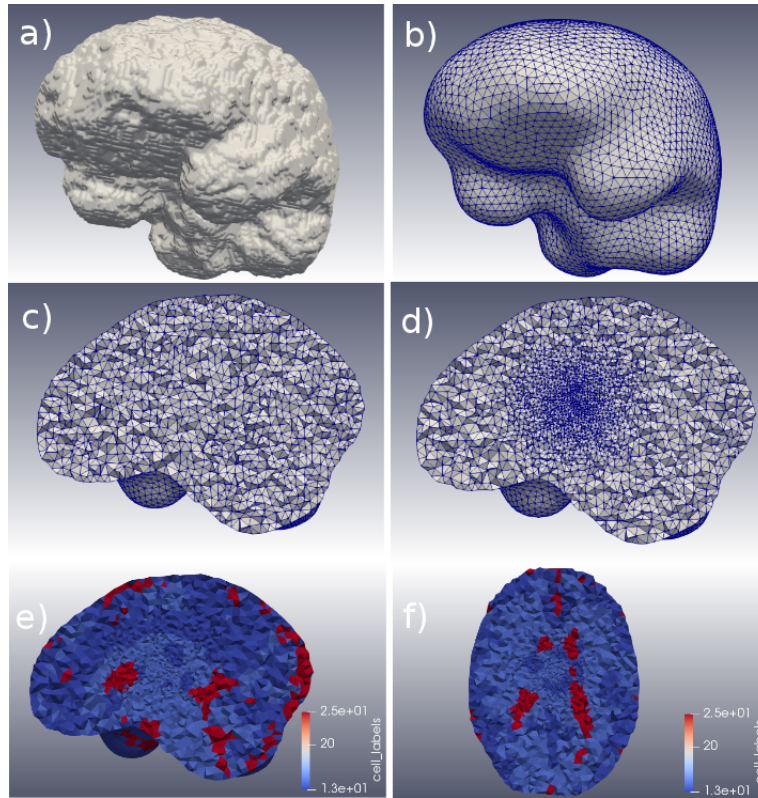
Figure 2: (a) External brain surface extracted from the segmented map; (b) remeshed and smoothed external surface; (c) tetrahedral mesh generated within the surface extracted from the medical images and then (d) conveniently refined in the area surrounding the tumour; (e-f) labelled mesh obtained from the refined mesh, in which to each cell is assigned a label depending on the cerebral tissue its barycenter belongs to: grey matter (blue), white matter (light blue), cerebrospinal fluid (red).
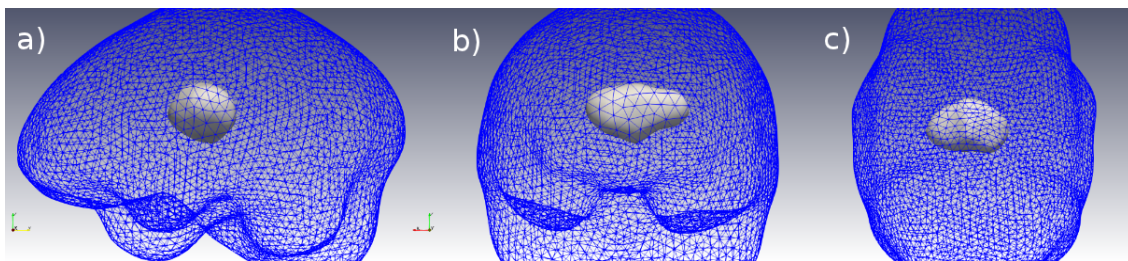

Figure 3: tumour extension at the PreSurg event. External brain (blue meshed surface) and tumour (light grey) surfaces from the segmented maps seen by different angles: x-normal view (a), y-normal view (b) and z-normal view (c).
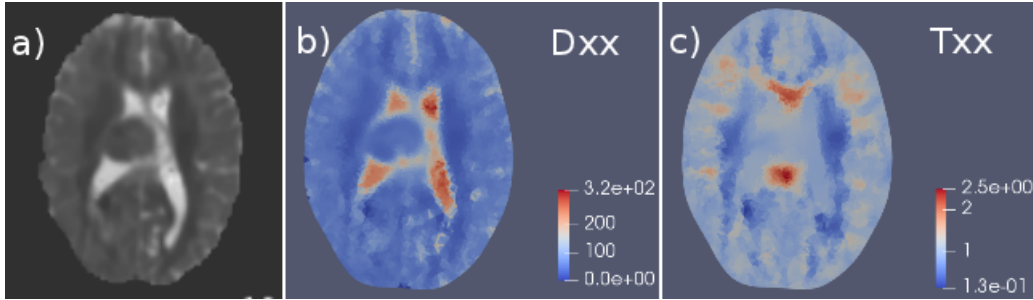
Figure 4: z-normal slices of the DTI data (a) and the meshes corresponding to the xx-components of the tensors $\boldsymbol{D}$ (b) and $\boldsymbol{T}$ (c).

within an admissible biological range. In particular, we initially take $E = 694$ Pa, $\nu = 0.08$ 1/day, $\nu_d = 0.04$ 1/day, $M_0 = 5000$ (Pa day)/mm^2, $\phi_e = 0.389$, $\epsilon = 0.35$ Pa$^{1/2}$mm, $\delta = 0.3$, $n_s = 0.07$ mM, $S_n = 10^4$ 1/day, $D_n = 86.4$ mm^2/day, $\delta_n = 8640$ 1/day, $k_n = 2$ mm^2/(mM day) except for the white matter in which $k_n = 8$ mm^2/(mM day). This set of parameters was proved [2] to reproduce a tumour expansion which follows a Gompertzian profile [36] with a GBM front velocity in the same order of magnitude of the maximal expansion speed reported in the literature, i.e. $0.09 - 0.11 mm/day$ [31].

We observe from Figure 1-b that some tumour aggregates seem to be still present in the PostSurg image inside the deformed area which was previously filled by the tumour mass. These regions appear as light white spots in Figure 1-b and are recognized by the segmentation process as belonging to the white matter tissue (colored in brown). The initial volume fraction of the tumour cells at the PostSurg event is thus determined in the following way:

i) we first define the characteristic function of the remaining tumour cells at the PostSurg event as the characteristic function of the white matter inside the domain of intersection between the tumour area at the PreSurg event (white meshes surface in Fig. 5a-c) and the area deformed after the tumour removal at the PostSurg event (green meshed surface in Fig. 5a-c);

ii) we multiply this characteristic function by a constant value representing the average volume fraction of the tumour clusters left after the operation (brown surface in Fig. 5a-c).

This average volume fraction of left tumour particles has been estimated in the following way: given a set of model parameters, we run a simulation starting from an initially small spherical tumour mass centered in the center of the tumour distribution manually segmented at the PreSurg event and growing in the CSF, until it reaches the same volume of the tumour's mass at the PreSurg event. In this situation the tumour concentration is expected to saturate at a peak value corresponding to the stationary solution of (1). By comparing T1-weighted and FLAIR MR images we found that the tumour mass at this stage is not very infiltrated inside the surrounding tissue, having a well defined border pushing against the ventricles. When the tumour is removed at the PostSurg event, the tumour particles that haven't been removed are identified as the remaining fragments infiltrated into the ventricle walls, thus having the same peak value of volume fraction.

By comparing the T1-weighted MR slice and the corresponding segmentation map in Figure 5 we noticed that most of the tumour particles left after the surgery are infiltrated inside the grey matter between the ventricles in the area filled by the tumour mass at the PreSurg event. A small fraction of tumour particles is also infiltrated at the boundary of the grey matter surrounding the ventricles in the same area.

Finally, once that the initial condition for the GBM volume fraction has been determined, we performed an adaptive procedure to tune the parameters of the model in order to obtain the
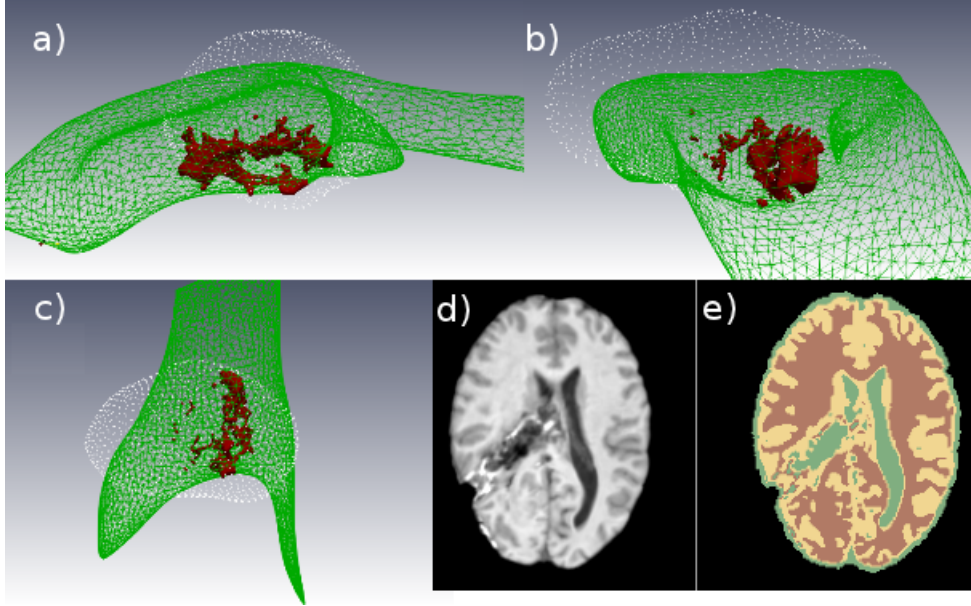
11

Figure 5: Initial concentration of the tumour distribution at the PostSurg event, calculated as the characteristic function of the white matter (brown) inside the PreSurg tumour area (white) and the area deformed after the tumour removal at the PostSurg event (green), multiplied by the average volume fraction of left tumour particles. a) Initial distribution from a x-normal view; b) a y-normal view; c) a z-normal view; d) Axial slices of the T1-weighted MR image (left) and the corresponding segmented map (right) at the PostSurg event.

best fit with the clinical data. In particular, we performed a sensitivity analysis by varying only k_n, M_0, ν and ν_d in order to obtain a tumour volume at the PreRad event which reproduces at least the 95% of the volume growth obtained from the MR images at the PreRad event (reported in Table 1).

We remark that the tumour boundary is conventionally represented by the hypersurface $\phi(\mathbf{x}, t) = 0.01$, and the volume of the tumour mass is calculated from the simulation results by considering the volumetric integral of the characteristic function of the set $\{\mathbf{x}|\phi(\mathbf{x}, t) > 0.01\}$.

We aimed at reproducing the 95% of the volume growth obtained from the MR images at the PreRad event for the best parameter fitting to be used in simulations. We found the following values: $k_n = 12$ mm^2/(mM day) in the white matter, $k_n = 3$ mm^2/(mM day) in the other brain tissues, $M_0 = 3900$ (Pa day)/mm^2, $\nu = 0.1$ 1/day, $\nu_d = 0.05$ 1/day.

In this case, the tumour concentration of an initial small spherical tumour mass reaches a peak value of about 0.61, that is chosen as the initial value ϕ_0 for the tumour volume fraction in simulations. The initial oxygen distribution $n_0(\mathbf{x}) := n(\mathbf{x}, 0)$ is the corresponding stationary solution of the nutrient governing equation:

$$-\nabla \cdot (\boldsymbol{D}\nabla n_0) = S_n(1 - n_0)(1 - \phi_0) - \delta_n \phi_0 n_0, \qquad (4)$$

where ϕ_0 is the initial tumour distribution. We also impose the following boundary conditions on the outer brain surface:

$$\nabla \phi \cdot \boldsymbol{n} = 0 \qquad \forall \mathbf{x} \in \partial\Omega, \qquad (5a)$$

$$\nabla \Sigma \cdot \boldsymbol{n} = 0 \qquad \forall \mathbf{x} \in \partial\Omega, \qquad (5b)$$

$$n = 1 \qquad \forall \mathbf{x} \in \partial\Omega \qquad (5c)$$

12

where $\boldsymbol{n}$ is the unit outer normal at the brain surface. In particular, a homogeneous Neumann condition on the cell volume fraction and on the chemical potential $\Sigma := f(\phi) - \epsilon^2 \Delta \phi$ is chosen to the spatial confinement of the skull bone, whilst a Dirichlet condition is taken for the nutrient as the physiological concentration of the oxygen in the brain.

4.3 Estimation of brain deformation and diffusion tensor at the PostSurg event

In Section 3 we highlighted a contraction of the brain ventricle containing the tumour mass at after its surgical removal. This poses a difficulty in the mesh definition, since it is not physically meaningful to associate to this deformed area the DTI data. In order to solve this issue, we manually identified the ventricle surfaces both at the PreSurg event and at the PostSurg event, as shown in Figure 1-f. Specifically, we assigned different labels to the region inside the ventricle surface at the PostSurg event (green area in Figure 1-f), that is called *deformed PostSurg region*, and the one between the ventricle surfaces at the PreSurg and PostSurg events (red area in Figure 1-f), denoted as *deformed PreSurg region*. The latter domain represents the region that is filled by CSF and tumour material at the PreSurg event and it is then occupied by brain tissue at the PostSurg event. We finally identified the *non-deformed region* as the outer domain that is not altered by the deformation. These domains are illustrated in Figure 6. Note that the width of the deformed PreSurg region, i.e., the area between the red meshed and the green meshed surfaces in Figure 6, defines locally the deformation undergone by the brain ventricle after the surgery. Accordingly, we established the following procedure to tune the values of the diffusion tensor at the PostSurg event. If the barycenter of a mesh cell belongs to the non-deformed region, we assign the values given by DTI data at the PreSurg event. If the cell mesh barycenter belongs to the deformed PreSurg or the deformed PostSurg regions, we average the diffusion values of each component, that is associated with the same tissue label in the PreSurg segmentation, over a spherical domain centered in the barycenter and with a given radius r. The radius is taken equal to the smallest value of the semiaxes of the tumour ellipsoid in the deformed PostSurg region, whereas in the deformed PreSurg region it is defined by $r = d_1 + d_2$ where d_1 and d_2 are the shortest distances between the cell mesh barycenter and the two surfaces bounding the deformed PreSurg region (highlighted as the red and the green meshes in Figure 6). These choices ensures that the DTI values are averaged over a domain that gives a meaningful physical representation of the local brain micro–structure at the PostSurg event.

The procedure outlined above allowed us to reconstruct the DTI information also in those region interested by deformation after tumour removal. This reconstruction is depicted in Fig. 7, displaying two x-slices of the component D_{yy} calculated from the DT images at the PreSurg event and the corresponding modified data at the PostSurg event. The comparison of these images allows to visualize how the diffusion components have changed in consequence of the ventricle deformation.

5 Results

In this section we investigate the tumour growth after the surgery and its response to radiotherapy. Simulation are performed starting at the PostSurg event (at time $t_0 = 0$ days), aiming at validating the numerical results against the tumour distribution observed by the MR images at the PreRad event (at time $t = 32$ days) and at the PostRad event (at time $t = 77$ days).

An adaptive time step, introduced in [2], has been implemented in order for the time step to satisfy the Courant-Friedrichs-Lewy condition $\Delta t < h_{min}/v_{max}$, being h_{min} the smallest edge
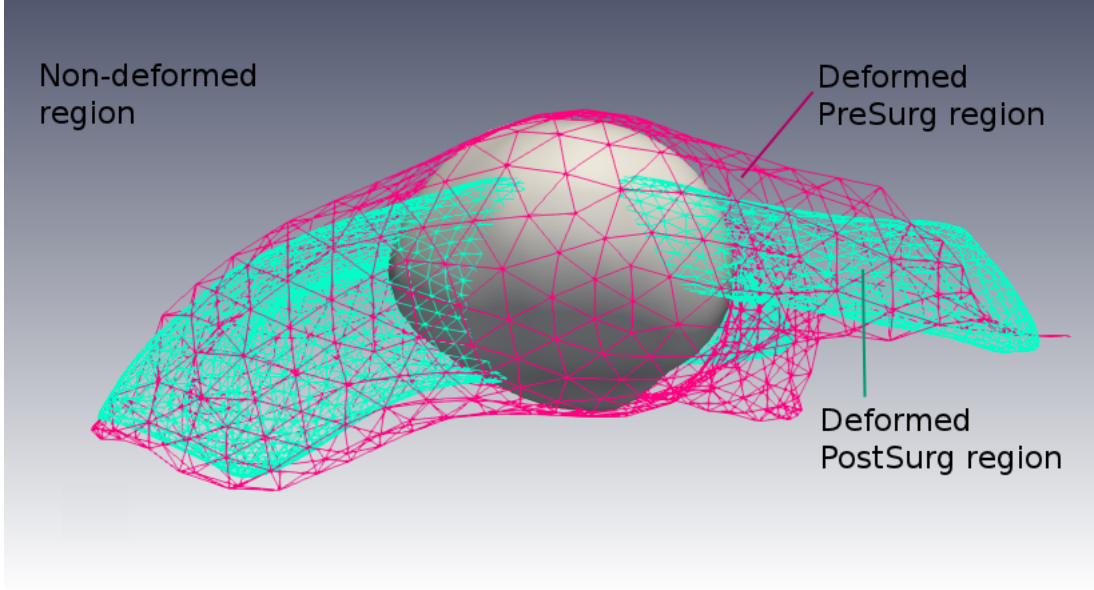
Figure 6: *Deformed PostSurg region*, defined as the region inside the inner surface mesh high-lighted in green color; *deformed PreSurg region*, defined as the region between the outer surface mesh in red color and the inner surface mesh in green color; *non-deformed region*, defined as the region outside the areas interested by the deformation.

length among the mesh cells and v_{max} the maximum on Ω of the tumour expansion velocity, defined as

$$v_{max} := \max_{\mathbf{x}_j} \left[\left(k_n n_s \boldsymbol{T} \nabla n - \frac{(1-\phi)^2}{M_0} \boldsymbol{T} \nabla \Sigma \right) \cdot \mathbf{n} \right] (\mathbf{x}_j), \tag{6}$$

where $\mathbf{x}_j$ are the spatial coordinates of the node j and $\mathbf{n}$ is the normal vector, proportional to $\nabla \phi$, to the hypersurfaces $\phi = c$, where c is a constant (which represents the direction locally orthogonal to the tumour front). In particular, we impose

$$\Delta t = \min \left(100 \cdot \frac{M_0}{E^2} \epsilon^2, \frac{h_{min}}{2 v_{max}} \right), \tag{7}$$

where $M_0 \epsilon^2 / E^2$ is the typical time scale for the spinodal decomposition dynamics of ϕ [12]. The basic temporal step is $\Delta t = 100 \cdot M_0 \epsilon^2 / E^2 \sim 0.1$ day.

In Figures 8-9 we show the time evolution of the mass and the volume of the tumour obtained by simulation. The mass of the tumour cells is defined as $\rho \int_\Omega \phi \, d\mathbf{x}$, with units of g. We observe that the mass of the tumour oscillates and decreases in correspondence to the application of the radiotherapy, indicated by red arrows in the figure, and starts to increase again after the therapy cycle. However, the total volume occupied by the multiphase tumour increases constantly from the PostSurg to the PostRad events, which means that the present tumour keep expanding in volume during the radiotherapy. In particular, the tumour volume calculated from simulations at the PreRad event is $6179.3 \, mm^3$, and the volume at the PostRad event is $10795.2 \, mm^3$. These values are compared to the ones obtained by the MR images reported in Table 1. Our results are in quantitative agreement with the experimental data at the PostRad event: the simulated tumour volume obtained is around 98% of the volume extracted from the MRI data. We also calculate the Jaccard index between the sets of the tumour support calculated by the simulation and by the MR images, reported in Figure 9 at the PreRad and the PostRad event.
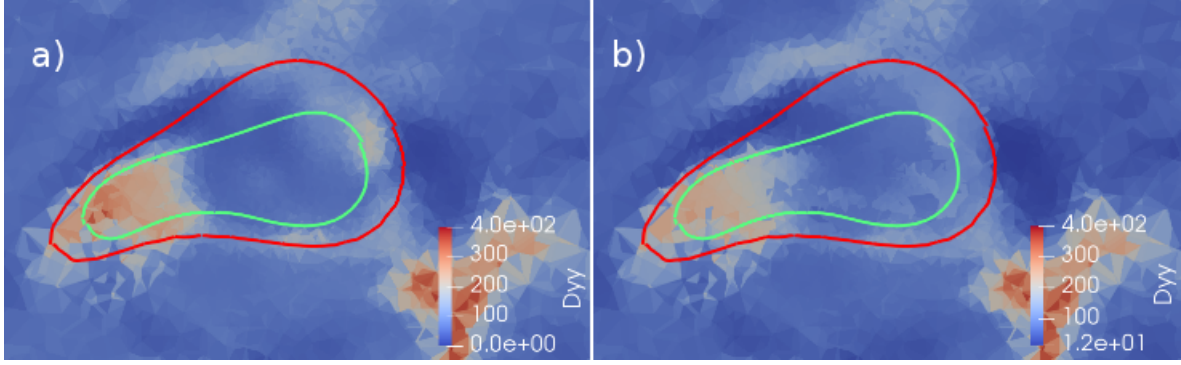
Figure 7: (a) x-slice of the component D_{yy} calculated from the DT images at the PreSurg event; (b) x-slice of the component D_{yy} calculated from the characterization of the brain tissues deformation at the PostSurg event. The contours of the deformed PreSurg and deformed PostSurg regions have been higlighted as red (outer) and green (inner) lines respectively.

The Jaccard index J between two sets of finite measure A and B is defined as

$$J := \frac{\int_\Omega \chi_{A\cap B}}{\int_\Omega \chi_{A\cup B}}, \tag{8}$$

where χ_S is the characteristic function of the set S which has value 1 for elements in the set and zero otherwise. This index has been used in [53] as a good metrics for model fitting, being a measure of the similarity of the two sets, which indicates how much they overlap everywhere. In our simulations the Jaccard index at the PostRad event is $J = 0.7116$. This value indicates a very good quantitative agreement between the tumour distribution predicted by the model and the one observed from the MRI data. The Jaccard index ranged between 0.45 and 0.66 in 3D simulations based on a parabolic anisotropic model based on DTI [53].

Moreover, the contour plots of the tumour concentrations at the PreRad and PostRad events are shown in Figure 9. We observe that the contours of the growing tumour according to the proposed model fit well with the contours obtained by the MR images both at the PreRad and the PostRad events. The qualitative agreement gets improved at the PostRad event. The simulation results show tumour infiltrations outside the tumour region identified in the MR image at the PreRad event. Figure 10 shows a z-slice of the tumour volume fraction calculated from the simulation results at the PostSurg, at the PreRad and the PostRad events, together with the tumour contours from the corresponding MR images.

From Figures 10-e and 10-f it can be observed a recidive of the tumour growth after the surgical removal at the PreRad event, and after the application of the radioterapic treatment at the PostRad event. In particular, while at the PreRad event the tumour is growing inside a region filled by CSF fluid, at the PostRad event the tumour is growing and infiltrating inside the grey matter surrounding it. We also observe from Figure 10-b that, at the PreRad event, a tumour infiltration outside the region outlined by the corresponding MR image is present in the simulation results. This infiltration is characterized by a smaller value of the concentration (around 0.3) than the value in the principal mass of the tumour (around 0.45). At the PostRad event this infiltration has became visible also in the MR image; in this case the simulated tumour concentration in Figure 10-c is contained inside the tumour region given by the MR image.

Figure 11 displays the evolution over time of the maximum expansion velocity $v_{\mathbf{max}}$ of the tumour front, defined in (6), obtained by the simulation results, from the PreRad to the PostRad events. We observe that $v_{\mathbf{max}}$ oscillates and decreases in correspondence to the application of the radiotherapy treatment, indicated by red arrows in the figure, and starts to increase after
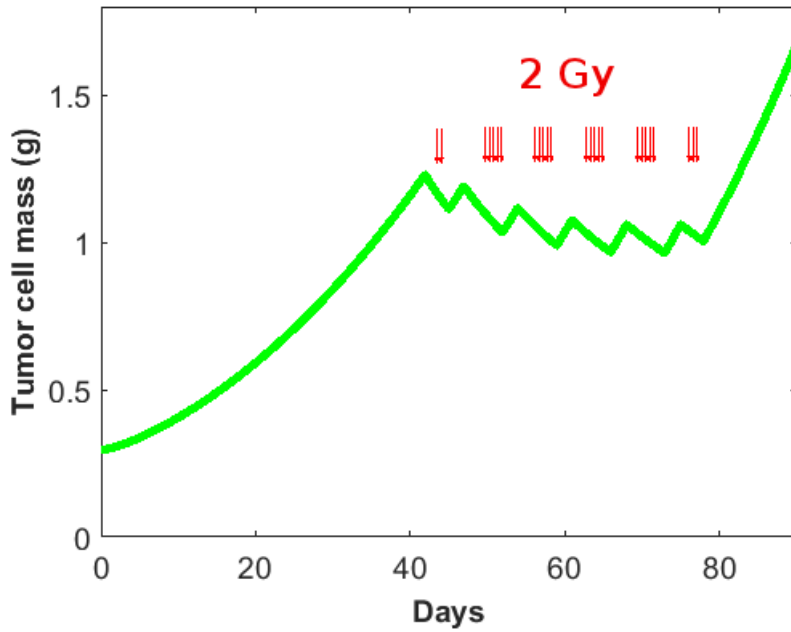
Figure 8: Time evolution of the mass of the tumour cells from the PostSurg to the PostRad events, with the application of the radiotherapy treatments of 2 Gy indicated as red arrows.

the therapy cycle. We note that before and after the radiotherapy treatment the expansion velocity reaches a value around $0.1mm/day$, which is in the same order of magnitude of the
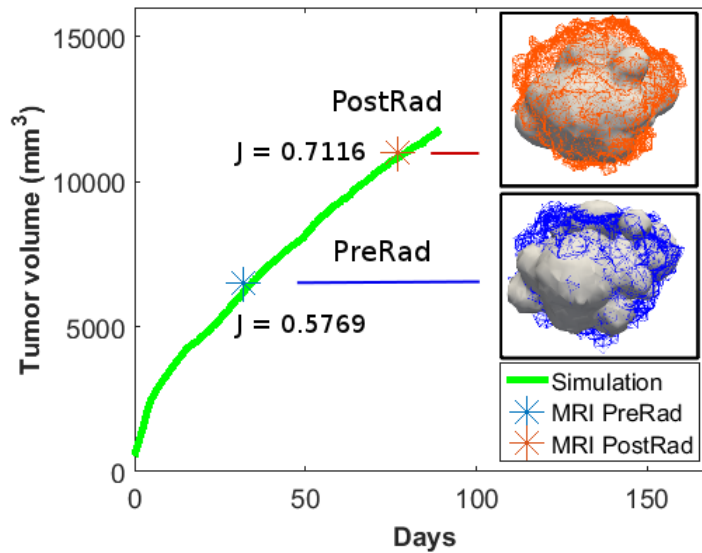

Figure 9: Evolution of the simulated tumour volume over time (green line), with indication of the Jaccard index J at the PreRad (blue marker) and PostRad (red marker) events. The insets display the simulated (light grey) and the observed tumour boundaries from MRI data (blue surface in PreRad, red surface in PostRad).
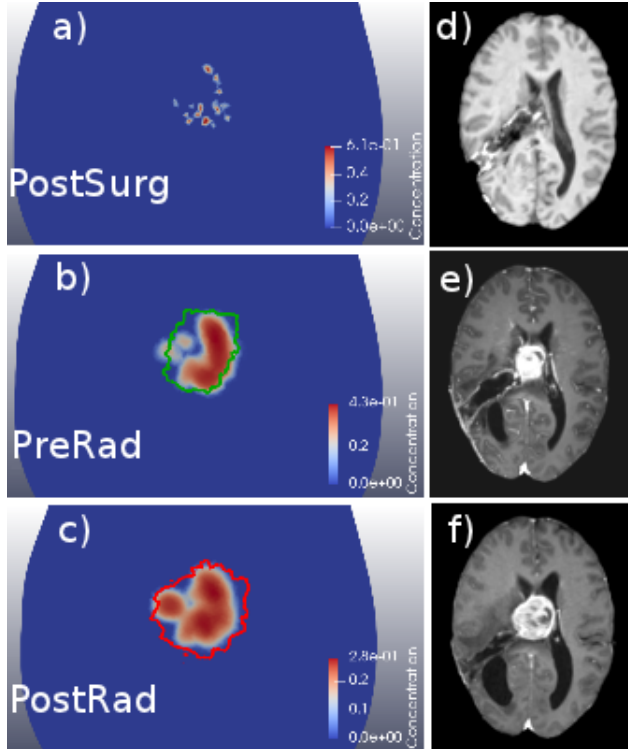
Figure 10: z-slice of the tumour concentration calculated from the simulations at the Post-Surg event (a), at the PreRad event (b) and at the PostRad event (c), overlapped with the corresponding contours of the tumour concentration from the MR images, highlighted in green (PreRad) and red (PostRad) color. Axial slices of the T1-weighted MR images at the PostSurg (d), PreRad (e) and PostRad (f) events.

maximal expansion speed reported in the literature, i.e. $0.09 - 0.11 mm/day$ [31] .

Moreover, in Figure 11 we report the average expansion velocity in the time period between the PreRad and the PostRad events, which we call v^*, calculated from the simulation results. This value is equal to $v^* = 0.068$ mm/day. We can compare this value with the corresponding velocity obtained from the analysis of the MR images.

At the top of Figure 11 we show the tumour contours manually segmented at the PreRad and the PostRad events. The experimental average velocities in the x, y and z directions can be obtained by calculating the difference of tumour semi-diameters along the coordinate axes of the tumour contours manually segmented at the PreRad and the PostRad events, divided by the time period of 45 days. Their values are 0.065 mm/day in the x direction, 0.048 mm/day in the y direction and 0.082 mm/day in the z direction, whose average value is 0.065 mm/day, which is in accordance with the value of 0.068 mm/day found in numerical simulations.

6   Discussion and Conclusions

This work used the diffuse-interface multiphase model recently proposed in [2] in order to simulate the clinical case study of a patient from the first diagnosis of a giant glioblastoma, to its surgical removal and the subsequent radiation therapies. The mechanical model consists in an evolutionary fourth-order partial differential equation with degenerate motility, describing the spreading over time of the tumour volume fraction, with a growth term that is coupled with a
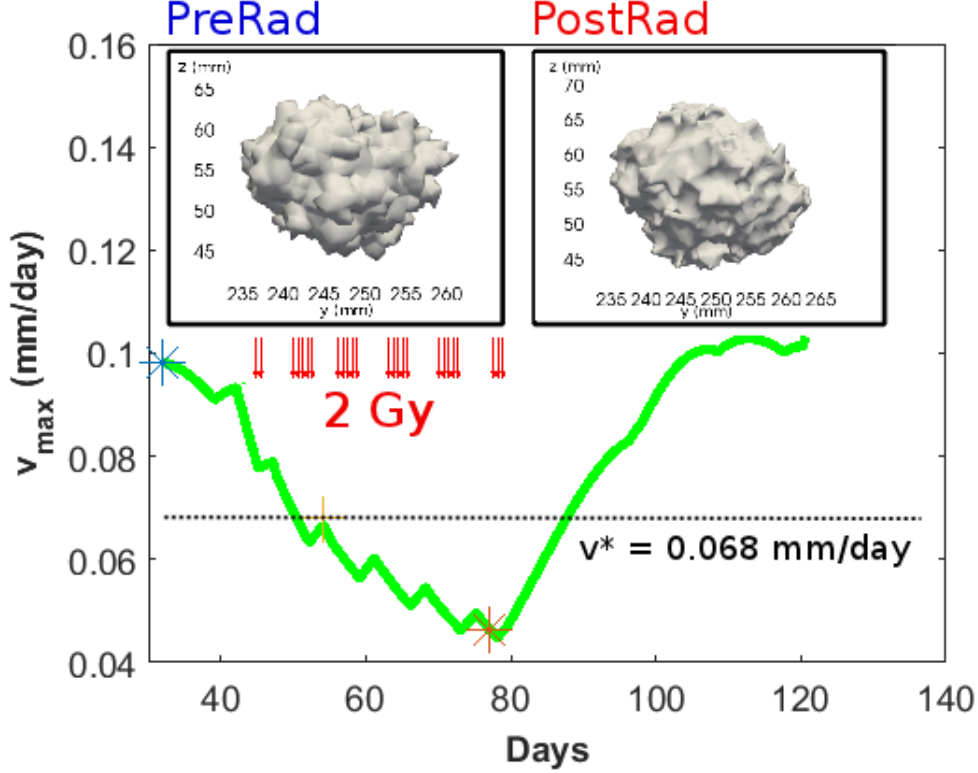
Figure 11: Evolution of the maximum expansion velocity $v_{\mathbf{max}}$ of the tumour front (green line) over time from the PreRad (blue marker) to the PostRad (red marker) events, with the application of the radiotherapy treatment of 2 Gy indicated as red arrows. The dashed line represents the average expansion velocity v^* in the time period between the PreRad and the PostRad events from the simulations. The insets show the tumour contours manually segmented at the PreRad (left) and the PostRad (right) events are also reported.

parabolic equation determining the diffusing oxygen within the brain. We developed a suitable finite element method for simulating the tumour evolution on the patient-specific brain geometry and micro–structure, that is reconstructed from MRI clinical data, aiming at predicting the recurrence pattern after the surgical resection. The model also includes a reaction term describing the effects of radiotherapy, that is simulated in accordance to the clinical schedule. Most of the model parameters were extracted directly from the patient MRI and DTI data, whilst a few were tuned in order to best fit the clinically detected tumour evolution within the physiological ranges found in literature. Notably, we successfully characterized the different brain tissues and the tumour location from MRI data, whilst we extrapolated from DTI data the heterogeneous and anisotropic nutrient diffusion parameters at given times of key clinical relevance, as well as the preferential directions of cell motion along white mater fiber bundles. The proposed approach represents a significant advance with respect to the state-of-the-art GBM models, since it takes into account both for the chemo-mechanical cues guiding cell migration in the patient-specific micro–structure of the simulated brain and for the multiphase composition of the tumour mass. Most importantly, the numerical results prove that the patient-specific mathematical model is able to predict the tumour recurrence in clinical case study. Indeed, we proved that the simulated contours of the recurrent tumour fit the corresponding boundaries observed in MRI data at given clinical times (i.e. just after surgical resection, before

and after the radiation therapy). Consistently with clinical data, the simulations pointed out a regression of the tumour mass in correspondence to the application of radiotherapy cycles, whilst the volume occupied by the tumour cells constantly increased with an average growth rate which is in agreement with the GBM expansion velocity reported in the literature [31] and calculated by the patient clinical data. The quantitative agreement is given by the 98% overlap calculated between the volume numerically simulated and the one detected from the neuroimaging data of the patient. Remarkably, our results display a higher Jaccard index of the tumour region after the application of therapies than any other model in the biomathematical literature [53], thus proving its ground-breaking potential for delivering accurate patient-specific predictions.

Another original contribution of this study is the definition of numerical strategy to take into account for the change of the DTI data before and after surgery, due to the registered brain deformation resulting from the release of mechanical stresses after tumour removal. Since the brain tissue tend to fill the remaining cavity, the correct alignment of fibers and their location cannot be inferred from the data acquired on the patient before the surgery was performed, such as done in [55, 57, 29, 14, 2]. Moreover, it is well known that the tumour modifies the fiber structure in the invaded area when spreading into the brain parenchyma [59, 45, 44, 62].

Future work will be focused on coupling the evolution of fibers alignment in the peritumoural area with the registered tissue deformations, with the aim to provide a quantitative tool towards an adaptive update of the clinical DTI data. Furthermore we will focus on refining the methods for fitting the model parameters through constrained optimization problems, and on the development of automated tumour segmentation tool, in order to avoid the manual segmentation that can introduce a bias and a human error into the process. The model will be finally applied on a large cohort of patients in order to test its reliability as a novel computation tool to assist the personalised clinical treatment.

In summary, this work represents an important proof of concept of the predictive ability of the model to describe the tumour progression and its response to therapies in a patient-specific manner. Such an original integration of neuroimaging data within the mathematical model has the potential to support medical doctors in the clinical evaluation of the optimal therapeutic strategy for every patient.

Acknowledgements

References

[1] A. Agosti, P. F. Antonietti, P. Ciarletta, M. Grasselli, and M. Verani, A Cahn-Hilliard type equation with application to tumour growth dynamics, Math. Meth. Appl. Sci., **40(18)**, 7598-7626 (2017).

[2] A. Agosti, C. Cattaneo, C. Giverso, D. Ambrosi, P. Ciarletta, A computational platform for the personalized clinical treatment of glioblastoma multiforme, preprint available at https://mox.polimi.it/publication-results/?id=702&tipo=add_qmox

[3] J.C.L. Alfonso, K. Talkenberger, M. Seifert, B. Klink, A. Hawkins-Daarud, K.R. Swanson, H. Hatzikirou, A. Deutsch, The biology and mathematical modelling of glioma invasion: a review. J R Soc Interface **14(136)** (2017).

[4] D. Ambrosi and L. Preziosi, On the closure of mass balance models for tumour growth, Math. Models Methods Appl. Sci. **12(5)**, 737-754 (2002).

[5] L. Antiga, M. Piccinelli, L. Botti, B. Ene-Iordache, A. Remuzzi, and D. A. Steinman, An image-based modeling framework for patient-specific computational hemodynamics, Med. Biol. Eng. Comput. **46**, 1097-1112 (2008).

[6] L. Barazzuol, N.G. Burnet, R. Jena, B. Jones, S.J. Jefferies, and N.F. Kirkby, A mathematical model of brain tumour response to radiotherapy and chemotherapy considering radiobiological aspects. Journal of Theoretical Biology, **262**(3), 553-565 (2010).

[7] P.J. Basser, J. Mattiello and D. Le Bihan, MR diffusion tensor spectroscopy and imaging, Biophys. J. **66(1)**, 259-267 (1994).

[8] W.L. Bi and R. Beroukhim, Beating the odds: extreme long-term survival with glioblastoma, Neuro. Oncol. **16**(9), 1159-1160 (2014).

[9] P-Y. Bondiau, O. Clatz, M. Sermesant, P-Y. Marcy, H. Delingette, M. Frenay, and N. Ayache, Biocomputing: numerical simulation of glioblastoma growth using diffusion tensor imaging, Phys. Med. Biol. **53**, 879-893 (2008).

[10] R. M. Bowen, Theory of mixtures, in: Continuum Physics, vol. 3, edited by A.C. Eringen (Academic Press, New York, 1976), Part I.

[11] H. M. Byrne, and L. Preziosi, Modelling solid tumour growth using the theory of mixtures, Math. Med. Biol. **20**,341-366 (2004).

[12] C. Chatelain, T. Balois, P. Ciarletta, and M. Ben Amar, Emergence of microstructural patterns in skin cancer: a phase separation analysis in a binary mixture, New J. Phys. **13(11)**,115013-115033 (2011).

[13] O. Clatz, M. Sermesant, P. Bondiau, H. Delingette, S. K. Warfield, G. Malandain, and N. Ayache, Realistic Simulation of the 3D Growth of Brain tumours in MR Images Coupling Diffusion with Biomechanical Deformation, IEEE Trans. Med. Imaging **24(10)**, 1334-1346 (2005).

[14] M.C. Colombo, C. Giverso, E. Faggiano, C. Boffano, F. Acerbi, and P. Ciarletta, Towards the Personalized Treatment of Glioblastoma: Integrating Patient-Specific Clinical Data in a Continuous Mechanical Model, PLoS ONE **10(7)**, e0132887 (2015).

[15] O. Commowick, N. Wiest-Daessl and S. Prima, Automated Diffeomorphic Registration of Anatomical Structures with Rigid Parts: Application to Dynamic Cervical MRI, Medical Image Computing and Computer-Assisted Intervention MICCAI 2012, Springer, Berlin, Heidelberg, 163-170 (2012).

[16] O. Commowick, N. Wiest-Daessle and S. Prima, Block-matching strategies for rigid registration of multimodal medical images, 2012 9th IEEE International Symposium on Biomedical Imaging (ISBI), IEEE, 700-703 (2012).

[17] D. Corwin, C. Holdsworth, R.C. Rockne, A.D. Trister, M.M. Mrugala, J.K. Rockhill JK, R.D. Stewart, M. Phillips, K.R. Swanson, Toward patient-specific, biologically optimized radiation therapy plans for the treatment of glioblastoma, PloS ONE **8**(11), e79115 (2013).

[18] P. Coupe,P. Yger, S. Prima, P. Hellier, C. Kervrann and . Barillot, An Optimized Blockwise Nonlocal Means Denoising Filter for 3-D Magnetic Resonance Images, IEEE Transactions on Medical Imaging **27(4)**, 425-441 (2008).

[19] V. Cristini, X. Li, J. S. Lowengrub, and S. M. Wise, Nonlinear simulations of solid tumour growth using a mixture model: invasion and branching, J. Math. Biol. **58**, 723-763 (2009).

[20] T. Deisboeck, M. Berens, A. Kansal, S. Torquato, A. Stemmer-Rachamimov, and E. Chiocca, Pattern of self organization in tumour systems: complex growth dynamics in a novel brain tumour spheroid model, Cell Prolif. **34(2)**, 115-134 (2001).

[21] C. Engwer, T. Hillen, M. Knappitsch, and C. Surulescu, Glioma follow white matter tracts: a multiscale DTI-based model, J. Math. Biol. **71(3)**, 551-582 (2015).

[22] C. Engwer, M. Knappitsch, C. Surulescu, A multiscale model for glioma spread including cell-tissue interactions and proliferation, Math. Biosci. Eng. **13**(2), 443-460 (2016).

[23] A. Giese, R. Bjerkvig, M. E. Berens, and M. Westphal, Cost of migration: invasion of malignant gliomas and implications for treatment, J. Clin. Oncol. **21(8)**, 1624-1636 (2003).

[24] P.G. Gritsenko, O. Ilina, P. Friedl, Interstitial guidance of cancer invasion, J. Pathol. **226**, 185-199 (2012)

[25] H. L. P. Harpold, E. C. Alvord Jr, and K. R. Swanson, The Evolution of Mathematical Modeling of Glioma Proliferation and Invasion, J. Neuropath. Exp. Neurol. **66(1)**, 1-9 (2007).

[26] H. Hatzikirou, A. Deutsch, C. Schaller, M. Simon, and K. Swanson, Mathematical modelling of glioblastoma tumour development: a review, Math. Models Methods Appl. Sci. **15(11)**, 1779-1794 (2005).

[27] R. Hdouin, O. Commowick, E. Bannier, B. Scherrer, M. Taquet, S.K. Warfield and C. Barillot, Block-Matching Distortion Correction of Echo-Planar Images With Opposite Phase Encoding Directions, IEEE Transactions on Medical Imaging **36(5)**, 1106-1115 (2017).

[28] C. Hogea, C. Davatzikos, and G. Biros, An image-driven parameter estimation problem for a reaction-diffusion glioma growth model with mass effects, J. Math Biol., 56(6), 793-825 (2008).

[29] A. Hunt, C. Surulescu, A Multiscale Modeling Approach to Glioma Invasion with Therapy, Vietnam Journal of Mathematics **45**(1), 221-240 (2016).

[30] S. Jbabdi, E. Mandonnet, H. Duffau, L. Capelle, K. R. Swanson, M. Pelegrini-Issac, R. Guillevin, and H. Benali, Simulation of Anisotropic Growth of Low-Grade Gliomas Using Diffusion Tensor Imaging, Magn. Reson. Med. **54**, 616-624 (2005).

[31] J. Johnson, M. O. Nowicki, C. H. Lee, E. A. Chiocca, M. S. Viapiano, S. E. Lawler, and J. J. Lannutti, Quantitative Analysis of Complex Glioma Cell Migration on Electrospun Polycaprolactone Using Time-Lapse Microscopy, Tissue Eng. Part C **15 (4)**, 531-540 (2009).

[32] L. J. Kaufman, C. P. Brangwynne, K.E. Kasza, E. Filippidi, V. D. Gordon, T. S. Deisboeck, and D. A. Weitz, Glioma expansion in collagen I matrices: analyzing collagen concentration-dependent growth and motility patterns, Biophys. J. **89(1)**, 635-650 (2005).

[33] E. Konukoglu, O. Clatz, P-Y B, H. Delingette, N. Ayache, Extrapolating glioma invasion margin in brain magnetic resonance images: Suggesting new irradiation margins, Medical Image Analysis **14**, 111-125 (2010).

[34] K.R. Kozak, and J.S. Moody, Giant cell glioblastoma: A glioblastoma subtype with distinct epidemiology and superior prognosis, Neuro. Oncol. *11*(6), 833-841 (2009).

[35] M. Lacroix, D. Abi-Said, D.R. Fourney, Z.L. Gokaslan, W. Shi, F. DeMonte, F.F. Lang, I.E. McCutcheon, S.J. Hassenbusch, E. Holland, K. Hess, C. Michael, D. Miller, and R. Sawaya, A multivariate analysis of 416 patients with glioblastoma multiforme: prognosis, extent of resection, and survival, Journal of Neurosurgery **95**(2), 190- 198 (2001).

[36] A. K. Laird, Dynamics of tumour growth, Br. J. Cancer **18(3)**, 490-502 (1964).

[37] M.J. McGirt, K.L. Chaichana, M. Gathinji, F.J. Attenello, K. Than, A. Olivi, J.D. Weingart, H. Brem, A.R. Quiñones-Hinojosa, Independent association of extent of resection with survival in patients with malignant brain astrocytoma: clinical article, Journal of Neurosurgery **110**(1), 156-162 (2009).

[38] P. Mosayebi, D. Cobzas, A. Murtha, M. Jagersand, tumour invasion margin on the Riemannian space of brain fibers, Med Image Anal. **16**(2), 361-373 (2012).

[39] M.L. Neal, A.D. Tanner, T. Cloke, R. Sodt, S. Ahn, A.L. Baldock, C.A. Bridge, A. Lai, T.F. Cloughesy, M.M. Mrugala, J.K. Rockhill, R.C. Rockne, and K.R. Swanson, Discriminating Survival Outcomes in Pa- tients with Glioblastoma Using a Simulation-Based, Patient-Specific Response Metric, PLOSone, **8**(1), 1-7 (2013).

[40] S. Ourselin, A. Roche, S. Prima and N. Ayache, Block matching: A general framework to improve robustness of rigid registration of medical images, Medical Image Computing and Computer-Assisted InterventionMICCAI 2000, Springer Berlin Heidelberg, 557-566 (2000).

[41] K. J. Painter and T. Hillen, Mathematical modelling of glioma growth: The use of Diffusion Tensor Imaging (DTI) data to predict the anisotropic pathways of cancer invasion, J. Theor. Biol. **323**, 25-39 (2013).

[42] S. Pieper, M. Halle, and R. Kikinis, 3D SLICER, Proceedings of the 1st IEEE International Symposium on Biomedical Imaging: From Nano to Macro **1**, 632-635 (2004).

[43] G. Powathil, M. Kohandel, S. Sivaloganathan, A. Oza, and M. Milosevic, Mathematical modeling of brain tumours: effects of radiotherapy and chemotherapy, Phys. Med. Biol. **52**, 3291-3306 (2007).

[44] S.J. Price, N.G. Burnet, T. Donovan, H.A. Green, A. Peña, N.M. Antoun, J.D. Pickard, T.A. Carpenter, J.H. Gillard, Diffusion tensor imaging of brain tumours at 3T: A potential tool for assessing white matter tract invasion?, Clin. Radiol. June;vol. **58**(6), 455-462 (2003).

[45] S.J. Price, A. Pena, N.G. Burnet, R. Jena, H.A. Green, T.A. Carpenter, J.D. Pickard, J.H. Gillard, Tissue signature characterisation of diffusion tensor abnormalities in cerebral gliomas, Eur. Radiol. **14**(10), 1909-1917 (2004).

[46] J.S. Rao, Molecular mechanisms of glioma invasiveness: the role of proteases, Nat. Rev. Cancer **3**, 489-501 (2003)

[47] R. Rockne, E. C. Alvord Jr, J. K. Rockhill, and K. R. Swanson, A mathematical model for brain tumour response to radiation therapy, J. Math. Biol. **58**, 561-578 (2009).

[48] R. Rockne, J. K. Rockhill, M. Mrugala, A. M. Spence, I. Kalet, K. Hendrickson, A. Lai, T. Cloughesy, E. C. Alvord Jr, and K. R. Swanson, Predicting the efficacy of radiotherapy in individual glioblastoma patients in vivo: a mathematical modeling approach, Phys. Med. Biol. **55**, 3271-3285 (2010).

[49] R. K. Sachs, L. R. Hlatky, and P. Hahnfeldt, Simple ODE Models of tumour Growth and Anti-Angiogenic or Radiation Treatment, Math. Comput. Model. **33**, 1297-1305 (2001).

[50] A. C. Shieh, Biomechanical forces shape the tumour microenvironment, Ann. Biomed. Eng. **39(5)**, 1379-1389 (2011).

[51] H. Si, TetGen, a Delaunay-Based Quality Tetrahedral Mesh Generator, ACM Trans. Math. Softw. **41(2)**, 11:1-11:36 (2015).

[52] C. Suarez, F. Maglietti, M. Colonna, K. Breitburd, G. Marshall, Mathematical modeling of human glioma growth based on brain topological structures: study of two clinical cases, PloS ONE **7**(6), e39616 (2012).

[53] A. Swan, T. Hillen, J. Bowman, and A. Murtha, A Patient-Specific Anisotropic Diffusion Model for Brain tumour Spread, Bull. Math. Biol. (2017).

[54] K. R. Swanson, E. C. Alvord Jr, and J. D. Murray, A quantitative model for differential motility of gliomas in grey and white matter, Cell Prolif. **33**, 317-329 (2000).

[55] K. Swanson, E. Alvord, J. Murray, Virtual resection of gliomas: effect of extent of resection on recurrence. Mathematical and Computer Modelling **37**(11), 1177-1190 (2003).

[56] K. R. Swanson, C. Bridge, J. D. Murray, and E. C. Alvord Jr, Virtual and real brain tumours: using mathematical modeling to quantify glioma growth and invasion, J. Neurol. Sci. **216**, 1-10 (2003).

[57] K. Swanson, R. Rostomily, E. Alvord, A mathematical modelling tool for predicting survival of individual patients following resection of glioblastoma: a proof of principle. British Journal of Cancer **98**(1), 113-119 (2008).

[58] J. Z. Wang, Z. Huang, S. S. Lo, W. T. C. Yuh, and N. A. Mayr, A Generalized Linear-Quadratic Model for Radiosurgery, Stereotactic Body Radiation Therapy, and High-Dose Rate Brachytherapy, Sci. Transl. Med. **2(39)**, 39ra48 (2010).

[59] U.C. Wieshmann, M.R. Symms, G.J. Parker, C.A. Clark, L. Lemieux, G.J. Barker, S.D. Shorvon, Diffusion tensor imaging demonstrates deviation of fibres in normal appearing white matter adjacent to a brain tumour, J. Neurol. Neurosurg. Psychiatry. **68**(4), 501-3 (2000)

[60] N. Wiest-Daessl, S. Prima, P. Coup, S.P. Morrissey and C. Barillot, Rician Noise Removal by Non-Local Means Filtering for Low Signal-to-Noise Ratio MRI: Applications to DT-MRI, Medical Image Computing and Computer-Assisted Intervention MICCAI 2008, Springer, Berlin, Heidelberg, 171-179 (2008)

[61] S. M. Wise, J. S. Lowengrub, H. B. Frieboes, and V. Cristini, Three-dimensional multi-species nonlinear tumour growth I - Model and numerical method, J. Theor. Biol. **253**, 524-543 (2008).

[62] B.P. Witwer, R. Moftakhar, K.M. Hasan, P. Deshmukh, V. Haughton, A. Field, K. Arfanakis, J. Noyes, C.H. Moritz, M.E. Meyerand, H.A. Rowley, A.L. Alexander, B. Badie, Diffusion-tensor imaging of white matter tracts in patients with cerebral neoplasm, J. Neurosurg. **97**(3), 568-575 (2002).

[63] Y. Zhang, M. Brady and S. Smith, Segmentation of brain MR images through a hidden Markov random field model and the expectation-maximization algorithm, IEEE Transactions on Medical Imaging **20(1)**, 45-57 (2001).

[64] J. Zhang, P. C. M. van Zijl, J. Laterra, A. Salhotra, B. Lal, S. Mori, and J. Zhou, Unique Patterns of Diffusion Directionality in Rat Brain tumours Revealed by High-Resolution Diffusion Tensor MRI, Magn. Reson. Med. **58**, 454-462 (2007).

[65] www.vtk.org.

MOX Technical Reports, last issues

Dipartimento di Matematica
Politecnico di Milano, Via Bonardi 9 - 20133 Milano (Italy)

14/2018   Cuffaro, M.; Miglio, E.; Penati, M.;Viganò, M.
Mantle upwelling driven by asymmetric sea-floor spreading at northern Mid–Atlantic ridge

15/2018   Simona, A.; Bonaventura, L.; Pugnat, T.; Dalena, B.
High order time integrators for the simulation of charged particle motion in magnetic quadrupoles

16/2018   Calissano, A.; Vantini, S.; Arnaboldi, M.
An elephant in the room: Twitter samplingmethodology.

13/2018   Gandelli, E.; Penati, M.;Quaglini, V.;Lomiento, G.; Miglio, E.; Benzoni, G.M.
A novel OpenSees element for single curved surface sliding isolators

12/2018   Dal Santo, N.; Deparis, S.; Manzoni, A.; Quarteroni, A.
Multi space reduced basis preconditioners for large-scale parametrized PDEs

11/2018   Delpopolo Carciopolo L.; Bonaventura L.; Scotti A.; Formaggia L.
A conservative implicit multirate method for hyperbolic problems

09/2018   Menafoglio, A.; Grasso, M.; Secchi, P.; Colosimo, B.M.
Profile Monitoring of Probability Density Functions via Simplicial Functional PCA with application to Image Data

10/2018   Menafoglio, A.; Gaetani, G.; Secchi, P.
Random Domain Decompositions for object-oriented Kriging over complex domains

08/2018   Bonaventura, L.; Casella, F.; Delpopolo, L.; Ranade, A.;
A self adjusting multirate algorithm based on the TR-BDF2 method

06/2018   Antonietti, P.F.; Mazzieri, I.
High-order Discontinuous Galerkin methods for the elastodynamics equation on polygonal and polyhedral meshes